Manuscript prepared for Atmos. Chem. Phys.
with version 2.1 of the LaTeX class copernicus.cls.
Date: 26 October 2014

Investigating the discrepancy between wet-suspension and dry-dispersion derived ice nucleation efficiency of mineral particles

Christopher Emersic[1], Paul J. Connolly[1], Stephen Boult[1], Mario Campana[2], and Zongyi Li[2]

[1]School of Earth, Atmospheric and Environmental Sciences, The University of Manchester
[2]School of Physics and Astronomy, The University of Manchester

Correspondence to: Paul J. Connolly
(p.connolly@man.ac.uk)

Abstract. Cloud chamber investigations into ice nucleation by mineral particles were reconciled with cold stage droplet freezing experiments. Kaolinite, NX-illite, and k-feldspar were examined, revealing k-feldspar to be the most ice active mineral particles in agreement with recent cold stage studies. The ice nucleation efficiency, as quantified using the *ice active site density* method were found to be in agreement with previous studies at the lower temperatures; however, at higher temperatures the efficiency was consistently higher than those inferred from cold stage experiments. Numerical process modelling of cloud formation during the experiments, using the cold-stage-derived parameterisations to initiate the ice phase, revealed the cold-stage-derived parameterisations to consistently under predict the number of ice crystals relative to that observed. We suggest the reason for the underestimation of ice in the model is that the slope of the cold-stage-derived *ice active site density* vs temperature curves are too steep, resulting in an underestimation of the number of ice crystals at higher temperatures during the expansion, which leads to evaporation of liquid water. Application of a coagulation model to the size distribution of mineral particles present in the samples that were used in the cold-stage-derived parameterisations revealed that there is a high probability that the mineral particles coagulate in suspension, which either removes them from the drops by sedimentation or reduces the particle surface area available for ice nucleation to take place. The implications are that the mineral particles may be more important than previously thought at high temperatures.

1 Introduction

Recently Hiranuma et al. (2014) determined ice nucleation efficiency of the NX-illite dust sample using a variety of methods. The methods were broadly classed as 'wet-suspension' methods, where mineral particles were put into water suspension before droplets of the suspension were cooled and frozen, or 'dry-dispersion' methods, where the mineral particles act as cloud condensation nuclei followed by freezing. Hiranuma et al. suggested that there was a discrepancy between the dry-dispersion methods and the wet-suspension methods at high temperatures, which they attributed to a change in chemical composition of the NX-illite mineral during dissolution in water.

Atmospheric mineral dust particles are comprised of several different minerals (e.g. Glaccum and Prospero, 1980; Kandler et al., 2007) and it is possible to determine their ice nucleation activity (e.g. Connolly et al., 2009, and others). However, there is much to be learned by investigating the ice nucleating ability of less complex 'pure minerals. Using a technique originally described by Vali (1971), Kaolinite and NX-illite have recently been examined in the immersion freezing nucleation mode (Murray et al., 2011; Broadley et al., 2012) and parameterisations of the ice-active surface site density have been put forward as have those for K-feldspar (Atkinson et al., 2013). These studies used 'wet-suspensions' to investigate ice nucleation by immersion freezing. They quantified the ice nucleation ability of the pure minerals using the ice-active site density concept, described as the number of ice active sites per unit surface area of dust, n_s, which was first presented by Connolly et al. (2009).

Murray et al. (2011) showed that the number of ice active sites on dust scales with the total surface area of dust in a drop; however, the total surface area available in their droplets was relatively large due to high particle concentrations in the dust suspension used to generate the droplets. In some cases the number concentrations exceeded 10^{17} m^{-3}, which equates to an inter particle spacing of $\sim 2\,\mu$m. At these high particle concentrations one might expect some interaction between neighbouring particles if they are able to come together and adhere due to the van der Waals interaction.

In nature, it is unlikely such high dust concentrations will be present in supercooled cloud droplets. Hence, the aim of this paper is to use a combination of laboratory experiments, data analysis and modelling to reconcile two different approaches for determining ice nucleation efficiency.

2 Experimental Set-up

Experiments were conducted in the Manchester Ice Cloud Chamber (MICC) fall tube, which has a diameter of 1 m and height of 10 m (additional details of the general facility are described in Connolly et al., 2012). The MICC and experimental set-up are shown in Figure 1

55 Initially, the chamber was pressure sealed and evacuated using two scroll pumps, capable of reducing pressure at a rate of approximately 1.4 hPa s^{-1}, to 200 hPa before refilling with filtered air. The filtered air had 10-20 cm^{-3} < 5 nm particles, with a total particle mass concentration < 0.01 μg m^{-3}. Volatile Organic Carbon, VOC, measurements by the Leicester Proton Transfer Reaction Mass Spectrometer always indicated VOC levels below detection

60 limits of approximately 1 ppb. This cleaning process was repeated a total of three times to reduce background aerosol concentration inside MICC to typically 20 cm^{-3}. The chamber was then cooled to the desired temperature, ranging from -12 to $-27\,^{\circ}$C depending on the experiment, and allowed to thermally equilibriate.

Prior to conducting the cloud formation experiments, a background experiment was per-

65 formed in which the pressure was reduced to 700 hPa to check that the remaining background aerosol in the chamber post-cleaning were not ice nuclei. Ice was only ever observed in low concentrations of a few cm^{-3} at the lowest temperatures and was attributed to homogeneous nucleation when the temperature during the pressure reduction process approached $-36\,^{\circ}$C. In the case where this was observed, the ice crystal concentration was substantially

70 lower than the resulting concentration in the later experiments where mineral dust particles were present.

Following the background experiment, a selected mineral dust was inserted into the chamber using a PALAS dust generator (RBG 1000 ID). This instrument uses particle free compressed air to separate and insert dust particles from a rotating brush which collects

75 them from a reservoir. The dust was inserted into the top of the chamber and allowed to homogenise; an initial measurement was taken using an Ultra High Sensitivity Aerosol Spectrometer (UHSAS), which uses an intracavity laser to measure aerosols in the size range (50 nm - 1000 nm) and a PALAS WELAS 2000 aerosol probe indicating total initial concentrations of approximately 1000 - 2000 cm^{-3}.

80 Liquid cloud formed as the pressure was reduced to 700 hPa from ice saturated conditions, and this was sampled with cloud probes, including the PALAS WELAS, Droplet Measurement Technologies (DMT) Cloud Droplet Probe (CDP), and Stratton Park Engi-

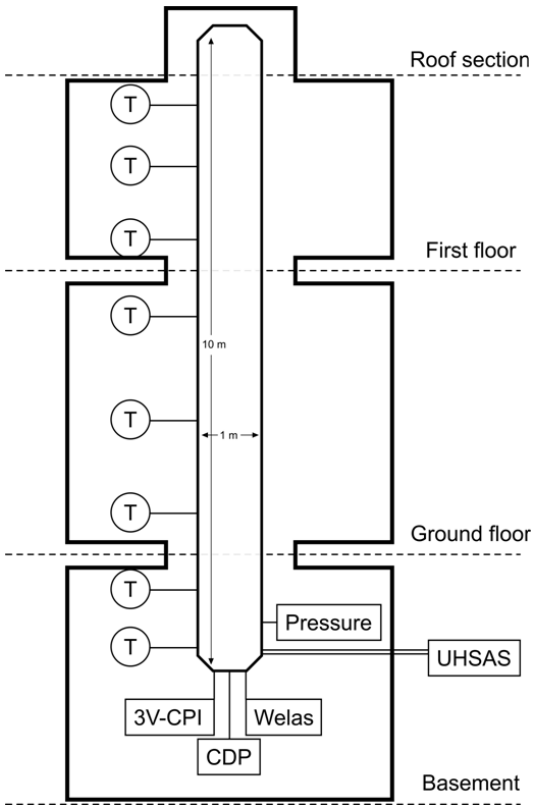

Fig. 1. A schematic of the MICC cold-rooms and chamber. Outer lines mark the outline of the outer wall of the cold rooms, with the MICC tube inside. Temperature probes are labeled with a 'T'. Pressure, and cloud properties are monitor in the bottom section of the chamber.

neering Company (SPEC) Cloud Particle Imager (CPI) 3V which includes a 2D-Stereo (2DS) probe. Internal chamber pressure was measured using a Lex 1 Keller pressure probe and the air temperature was measured using calibrated type K thermocouples arranged along the height of and in the centre of the cloud chamber. Several repeat pressure reduction cycles were performed once dust was inserted; after each experiment, the chamber was filled back to ambient pressure using the clean air system described above. A set of experiments for each dust was performed at both higher and lower temperature, and in total, Kaolinite, Feldspar, and Illite were used, giving a total of 6 experiment sets comprising ~ 4 runs per set (a total of ~ 24 depressurisations, not including background runs).

3 Observations

Figure 2 and Figure 3 show the results of the two first experimental runs on K-feldspar—the same sample used in the Atkinson et al. (2013) study. Figure 2 was conducted with the initial temperature equal to -12°C and expansion of the air to 700 hPa resulted in the temperature decreasing to ~ -19°C. The middle plot of Figure 2 shows the time evolution of the measured size distribution from the CDP. Mineral particles are visible at the start of the experiment at sizes up to $\sim 10\,\mu$m, whereas ~ 25 s into the experiment a cloud of droplets grows as noted from the brighter colours. Following the formation of drops, ice crystals are formed and grow to large sizes. The cloud of drops evaporates at ~ 200 s due to the Bergeron-Findeison process, following which the ice crystals are able to persist to ~ 300 s. The bottom plot of Figure 2 shows that the drop concentration measured with the CDP reaches ~ 2000 cm^{-3}. The ice concentration determined by the 3V-CPI (red-line) agrees very well with the concentrations of particles greater than $18\,\mu$m as measured with the CDP (blue line), thus giving confidence in our measurements of ice crystal concentration. The blue-dashed line is the concentration of particles greater than $35\,\mu$m measured with the 3V-CPI. It should be noted the reason this is greater than the concentrations of particles greater than $18\,\mu$m measured with the CDP is because the 3V-CPI often over-sizes out of focus images of droplets (Connolly et al., 2007).

Figure 3 shows the results of the first run of K-feldspar at an initial temperature of $-21\,$°C. During the expansion the air temperature reduced to $\sim -28\,$°C. The CDP showed evidence of droplets forming for a brief period at ~ 40 s in to the experiment (middle plot and black line on bottom plot). However, the droplets lasted for a brief period (less than ~ 40 s). The 3V-CPI concentration is lower than the CDP concentration of particles greater than $18\,\mu$m (blue line); however, in this experiment it was difficult to discriminate the ice crystals on shape alone because the ice crystals appeared somewhat rounded due to the lack of vapour growth. Furthermore, the concentrations of particles greater than $18\,\mu$m, measured with the CDP, and those measured with the 3V-CPI greater than $35\,\mu$m are in good agreement. For this experiment it was more accurate to use these two measurements for the ice crystal concentrations.

Similar plots are shown in Figures 4 and 5, but for kaolinite at -19°C and -25°C respectively. In Figure 4 (middle plot) a cloud of droplets forms for ~ 50 seconds before evaporating to leave an ice cloud. It is more difficult to see from the CDP data that the ice

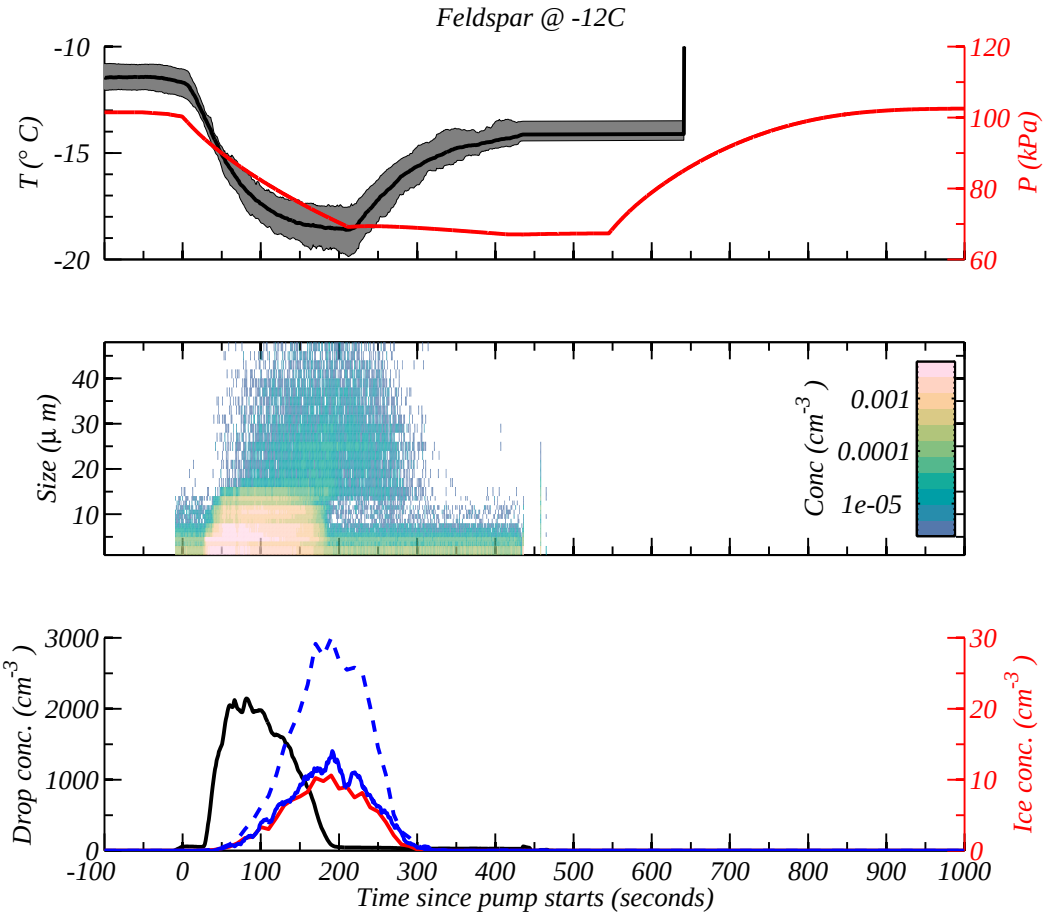

Fig. 2. Feldspar mineral particles at -12°C. Top shows the temperature in the chamber (black line, left axis) and the pressure (red line, right axis). The black line is the mean of temperature probes, while the grey shading demarks the range in measured temperatures across all probes. Middle plot shows the size distribution as measured with the CDP instrument. Bottom plot shows: (1) the drop concentration measured with the CDP (black line, left axis); (2) the concentration of particles larger than the main droplet mode (solid blue line, right axis); (3) the ice crystal concentration measured with the 3V-CPI (red line, right axis); (4) the concentration of particles larger than 35 microns with the 3V-CPI (dotted blue).

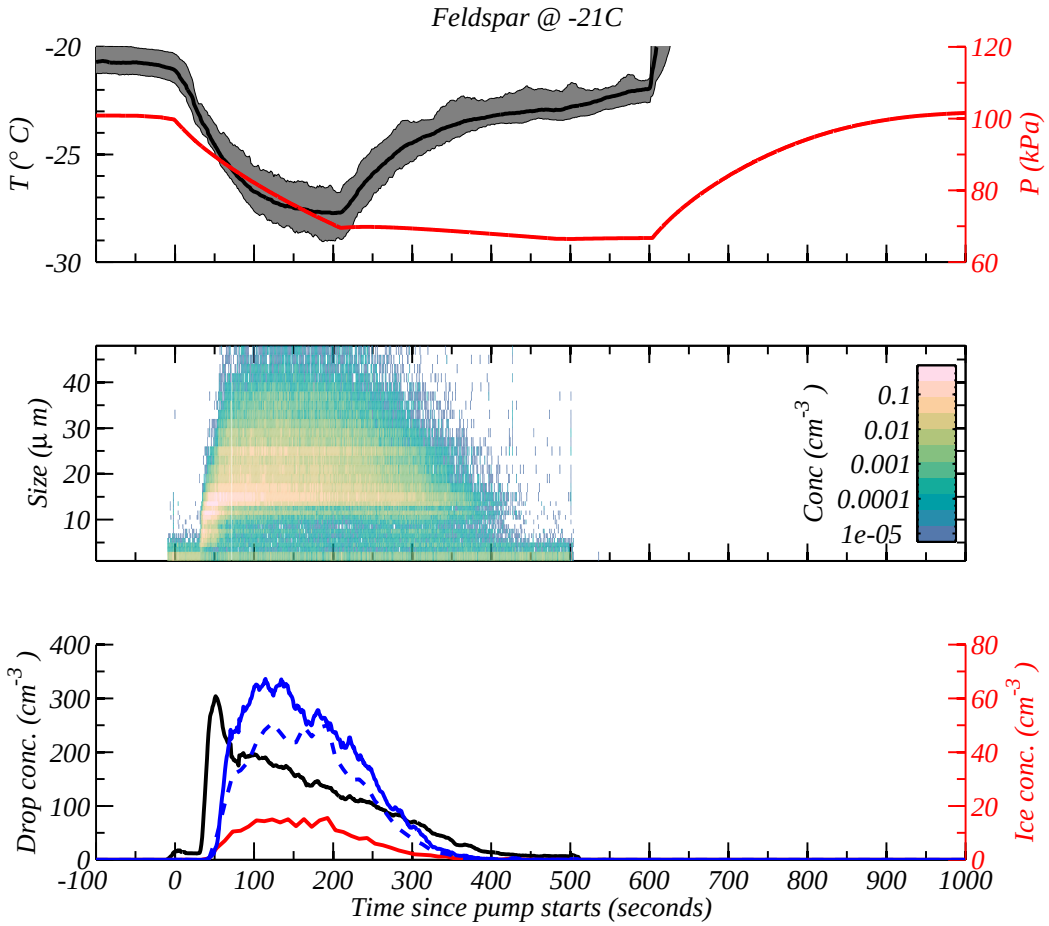

Fig. 3. Same as Figure 2, but for feldspar at -21°C.

cloud nucleates after the drops form, because the optical sizes of the ice crystals overlap with the optical sizes of the largest kaolinite particles; nevertheless the 3V-CPI data indicated that this was the case (not shown). The bottom plot of Figure 4 shows that the 3V-CPI derived ice crystal concentration (red line) is about a factor of two smaller than the particles larger than 18 μm from the CDP (and those larger than 35 μm from the 3V-CPI, blue lines); this is because some of the ice crystal are too small to be able to unequivocally classify them as ice crystals on their shape alone, so we slightly underestimate the ice concentration here.

Figure 5 middle shows that the kaolinite particles nucleate ice in the absence of a cloud of droplets. In fact, the droplets are too small to see with the CDP: the humidity in the chamber was close, and likely above water saturation. The drops are not visible because the Bergeron-Findeison process acts rapidly in this experiment, leaving the drops with little time to grow. The drop mode became more visible with repeat experiments (not shown):

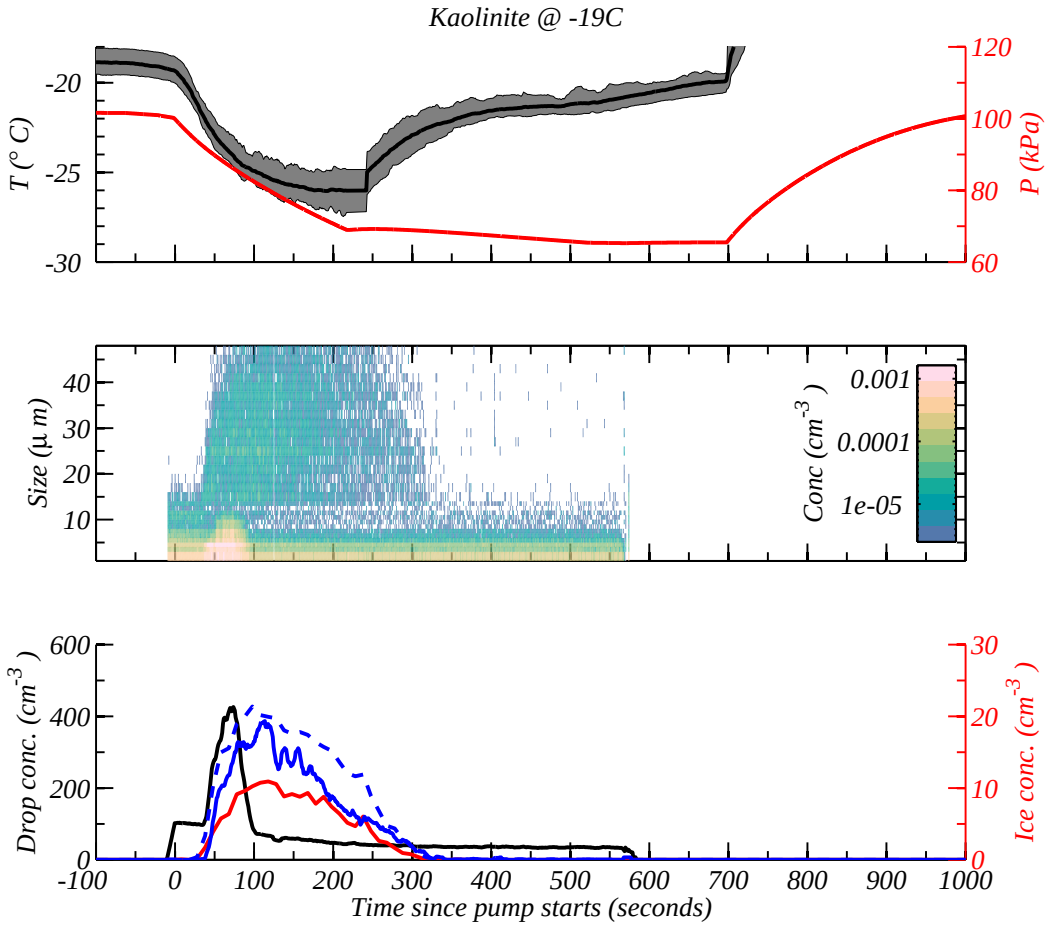

Fig. 4. Same as Figure 2, but for kaolinite at -19°C.

(a) because the particle concentration was diluted and (b) because the largest, most IN active particles were used up, which enabled the drops to grow to larger sizes. As for the experiment at higher temperature the 3V-CPI derived ice crystal concentration was below that of the concentrations that were derived on size alone from the CDP and 3V-CPI (solid blue and dashed blue lines respectively). Again this is because the particle sizes were often too small to unequivocally classify them as ice; hence, we classified the ice based on size for these runs (blue lines).

Finally, we have similar plots for the NX-illite sample in Figures 6 and 7. In Figure 6 (top) we see that the initial temperature was -15°C, which decreased to ~ -23°C throughout the experiment. The middle plot shows that the droplet mode was of fairly long duration, lasting up to $\sim$ 300s and that there were relatively few ice crystals (as noted from the few speckles above 18 μm in size). The 3V-CPI and CDP derived ice concentrations agree reasonably

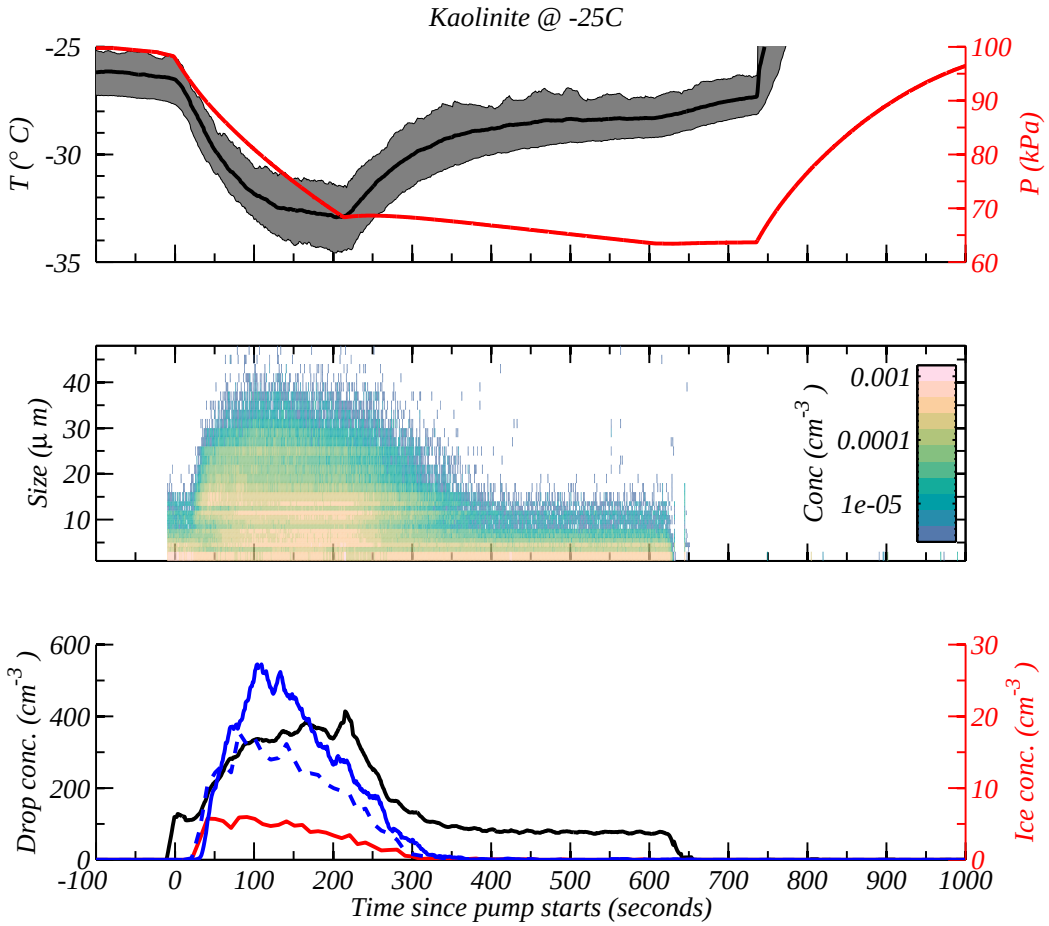

Fig. 5. Same as Figure 2, but for kaolinite at -25°C.

well in this case; however, the concentration of particles larger than 35 μm as measured with the 3V-CPI is larger than those larger than 18 μm measured with the CDP. The reason for this is that the 3V-CPI has a tendency to over estimate the size of the drops when they are out of focus. Drop concentrations were $\sim$ 2000 cm^{-3}.

For NX-illite at -25°C in Figure 7 the picture is similar to K-feldspar and kaolinite at the lower temperatures. There is no visible drop mode and the ice crystal concentration inferred from the 3V-CPI images is lower than those inferred from the CDP and 3V-CPI on size alone (bottom plot). The drop mode was visible in later expansions, when the most efficient ice nuclei had been used up and thus removed from the chamber (not shown). The reason the 3V-CPI derived ice crystal concentrations were smaller than the CDP and 3V-CPI concentrations based on size is again due to the ice crystals not developing distinct facets because there are many of them; hence, for these experiments we classified the ice on size

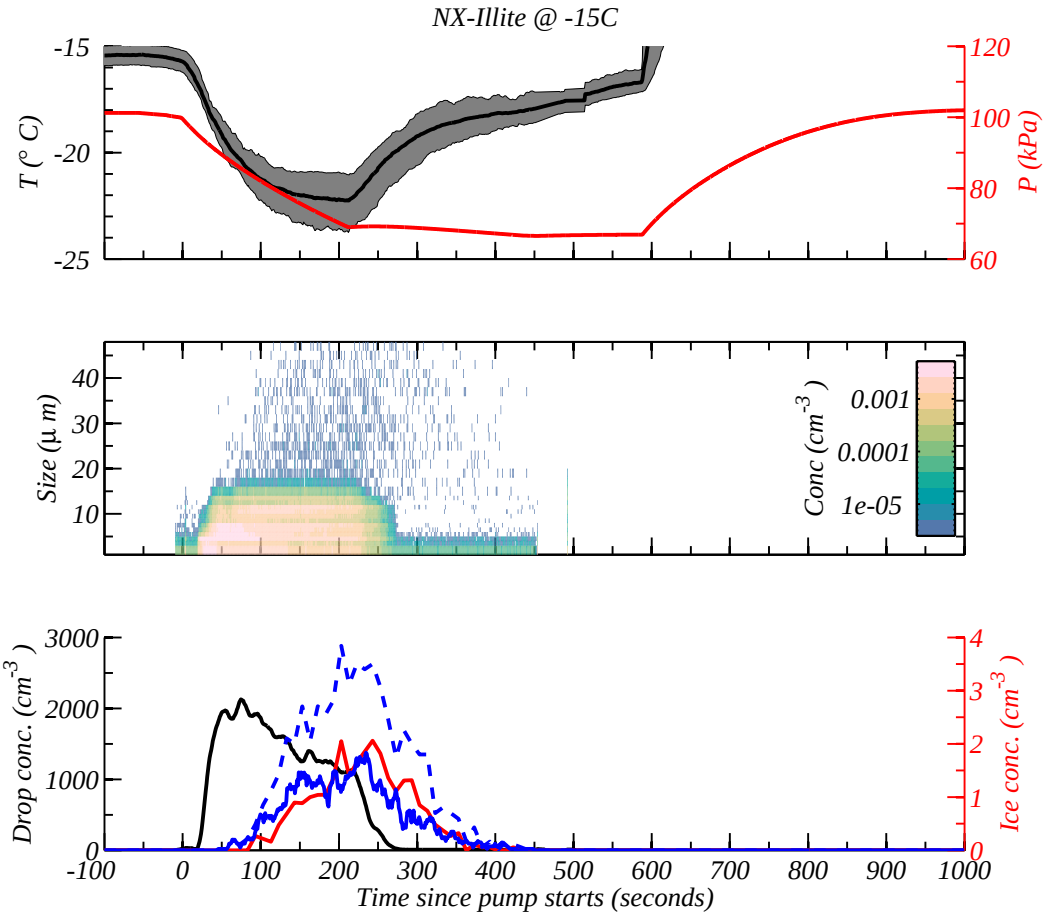

Fig. 6. Same as Figure 2, but for illite at -15°C.

alone (blue lines). It is noteworthy that drop concentrations were $\sim$ 500 cm^{-3}, which is lower than the aerosol by a factor of $\sim$ 3. NX-illite had the highest specific surface area and we suspect that this decreases its effectiveness as a cloud condensation nucleus (CCN), and it perhaps even acts in the adsorption mode of CCN activation rather than in the mode described by Köhler theory (e.g. Kumar et al., 2008).

4 Analysis

To compare our dry dispersion chamber observations with wet suspension cold stage methods (e.g. Murray et al., 2011; Broadley et al., 2012; Atkinson et al., 2013) we used two main

[1]CDP used to determine ice concentrations for this experiment because the concentrations were high and hence the ice crystal sizes were small.

Table 1. Table showing summary of experimental results. Multiple rows indicate the expansion number on the same mineral particle sample after refilling to 1000 hPa. Geometric surface areas were obtained through integration of the size distribution assuming spherical particles. Errors in ice crystal concentration are calculating using Poisson counting statistics at the 0.05 level of significance.

Mineral sample	ice conc. (cm^{-3})	N (cm^{-3})	D_m (μm)	$\ln \sigma_g$	Geometric surface area (m^{-1})
K-feldspar @ $-12°$ C	8.96 ± 0.15	[1700 , 45]	[0.32 , 2.8]	[0.3 , 0.55]	1.99×10^{-3}
	6.31 ± 0.13	[1200 , 15]	[0.32 , 2.8]	[0.5 , 0.55]	1.25×10^{-3}
	4.53 ± 0.11	[800 , 4]	[0.32 , 2.8]	[0.5 , 0.45]	5.75×10^{-4}
	2.56 ± 0.08	[400 , 3]	[0.32 , 2.8]	[0.5 , 0.65]	3.44×10^{-4}
K-feldspar @ $-21°$ C[1]	47.16 ± 0.35	[1000 , 20]	[0.32 , 2.8]	[0.5 , 0.8]	1.41×10^{-3}
	53.39 ± 0.38	[600 , 20]	[0.33 , 1.0]	[0.45 , 1.5]	7.03×10^{-4}
	32.56 ± 0.29	[300 , 20]	[0.33 , 1.0]	[0.45 , 1.4]	5.42×10^{-4}
	27.05 ± 0.27	[200 , 1]	[0.33 , 1.0]	[0.45 , 0.8]	1.10×10^{-4}
Kaolinite@ $-19°$ C	9.51 ± 0.16	[500 , 90]	[0.45 , 2.8]	[0.4 , 0.6]	4.35×10^{-3}
	1.52 ± 0.06	[300 , 20]	[0.45 , 2.8]	[0.4 , 0.5]	1.13×10^{-3}
	0.34 ± 0.03	[200 , 8]	[0.45 , 2.8]	[0.4 , 0.5]	5.50×10^{-4}
	0.20 ± 0.02	[100 , 15]	[0.45 , 2.8]	[0.4 , 0.55]	7.23×10^{-4}
	0.06 ± 0.01	[50 , 5]	[0.45 , 2.8]	[0.4 , 0.8]	2.81×10^{-4}
Kaolinite@ $-25°$ C	5.29 ± 0.12	[500 , 90]	[0.4 , 3]	[0.4 , 0.6]	4.55×10^{-3}
	8.43 ± 0.15	[375 , 60]	[0.45 , 3]	[0.4 , 0.6]	3.21×10^{-3}
	8.59 ± 0.15	[250 , 40]	[0.5 , 2.8]	[0.4 , 0.65]	2.11×10^{-3}
	8.78 ± 0.15	[150 , 25]	[0.45 , 2.8]	[0.4 , 0.8]	1.28×10^{-3}
	4.69 ± 0.11	[50 , 15]	[0.45 , 2.8]	[0.5 , 0.8]	7.26×10^{-4}
Illite@ $-15°$ C	1.59 ± 0.07	[1400 , 15]	[0.28 , 2.6]	[0.25 , 0.5]	5.10×10^{-4}
	0.182 ± 0.02	[700 , 5]	[0.27 , 2.6]	[0.28 , 1.3]	1.92×10^{-4}
	0.037 ± 0.01	[400 , 2]	[0.27 , 2.6]	[0.48 , 0.5]	1.73×10^{-4}
	0.021 ± 0.03	[250 , 3]	[0.27 , 2.6]	[0.48 , 2]	1.50×10^{-4}
Illite@ $-25°$ C	8.04 ± 0.15	[1700 , 25]	[0.28 , 3]	[0.45 , 0.5]	1.51×10^{-3}
	10.36 ± 0.17	[1500 , 20]	[0.28 , 3]	[0.45 , 1]	1.27×10^{-3}
	10.92 ± 0.17	[800 , 15]	[0.28 , 3]	[0.45 , 1.6]	7.14×10^{-4}

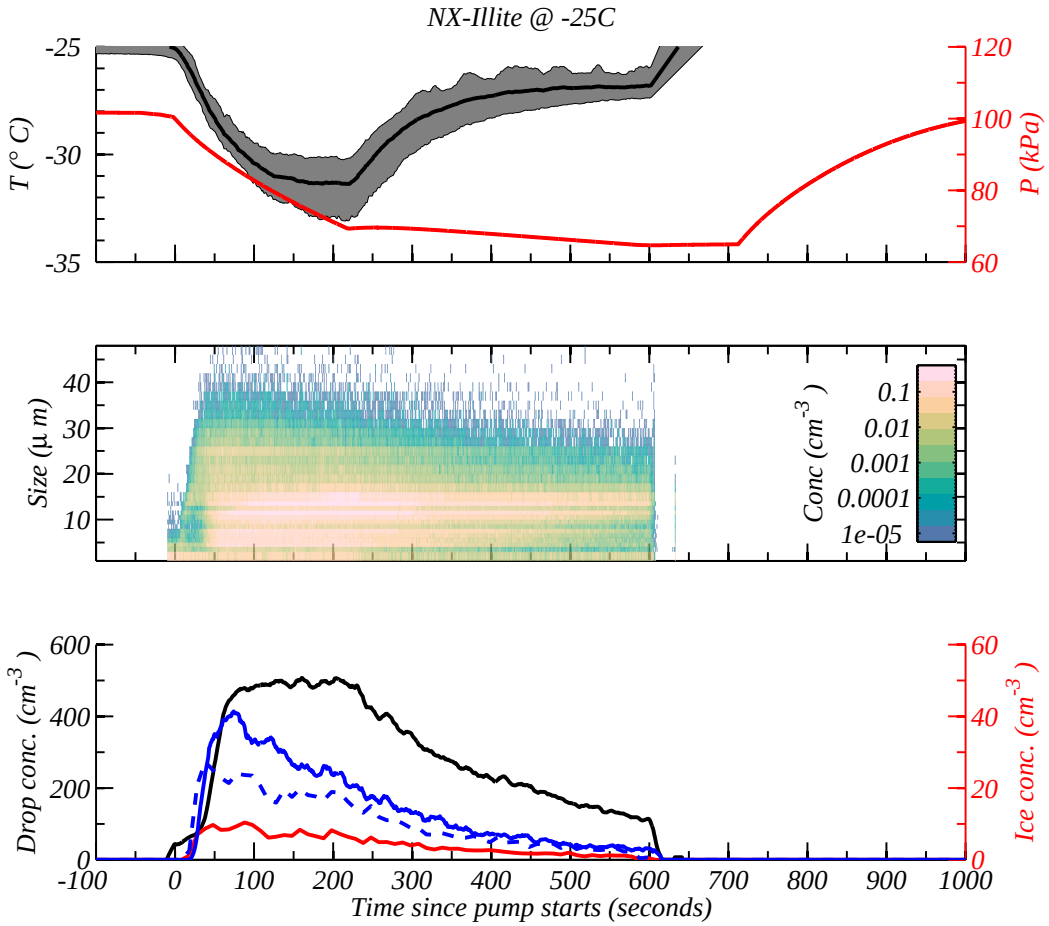

Fig. 7. Same as Figure 2, but for illite at -25°C.

approaches. Firstly we calculated values of the ice-active-surface-site density, or n_s, using our data and plotted them on the same graph as existing data taken using cold stages (see Section 4.1). Secondly the Aerosol-Cloud-Interactions Model (ACPIM) (Connolly et al., 2012) was used to simulate the MICC cloud chamber experiments. In this model, the freezing parameterisations of Murray et al. (2011); Broadley et al. (2012); Atkinson et al. (2013) were used to compare ice concentrations expected with those observed. ACPIM is discussed and the analysis is presented in Section 4.2.1.

4.1 Calculating n_s directly from the data

We calculated n_s directly from the data in the following way. The result of the n_s concept is that the fraction of drops, f, containing surface area, A, that are frozen at temperature, T,

is described by the factor:

$$f = 1 - \exp\left(-An_s\left[T\right]\right) \tag{1}$$

Hence, for an input dust particle size distribution, $\frac{dN}{dD}$, where all particles are hygroscopic, or take up at least a mono-layer of water, we write the number of ice crystals that are nucleated as:

$$N_{ice} = \int_{D_{min}}^{D_{max}} \frac{dN\left(D\right)}{dD}\left(1 - \exp\left(-An_s\left[T\right]\right)\right) dD \tag{2}$$

Here D_{min} and D_{max} are the minimum and maximum particle size in the mineral particle size distribution.

The value used for A in Equation 2 is the surface area of a sphere multiplied by a factor to yield the BET specific surface area (see Table 3). We calculate n_s from our data using Equation 2 with an iterative method. Firstly, we use an initial guess of n_s and evaluate the integral in Equation 2. We then compare the calculated value of N_{ice} with the measured value. This process is repeated with updates to n_s until convergence is found.

Another way of estimating n_s (e.g. Niemand et al., 2012; Hiranuma et al., 2014) has been to divide the measured ice crystal number concentration by the surface area of the aerosol size distribution, as measured at the start of the experiment (with a pressure correction for dilution during the expansion):

$$n_s \cong \frac{N_{ice}}{\pi \int_{D_{min}}^{D_{max}} D^2 \frac{dN(D)}{dD} dD} \tag{3}$$

However, this method can lead to an underestimation of n_s because it does not take into account the removal of surface area from the dust size distribution as they nucleate ice.

The values of n_s derived using the iterative method are shown in Figure 8. We have chosen to plot each experimental run as a single data point. Since the ice crystal concentrations are measured with time we could use a single experiment for multiple data points as is typically done in other studies (e.g. Niemand et al., 2012; Hiranuma et al., 2014); however, we have more confidence in the accuracy of the experimental averaged data points. It can be seen that at the higher temperatures, values from the chamber (using dry dispersion) are significantly larger than those taken from cold stages (using wet suspension). This effect has been noted for NX-illte in the recent study by Hiranuma et al. (2014).

4.2 Process Modelling

The application of ACPIM to understand and interpret the implications observations is described in Section 4.2.1, below. The discrepancies noted in Figure 8 prompted us to un-

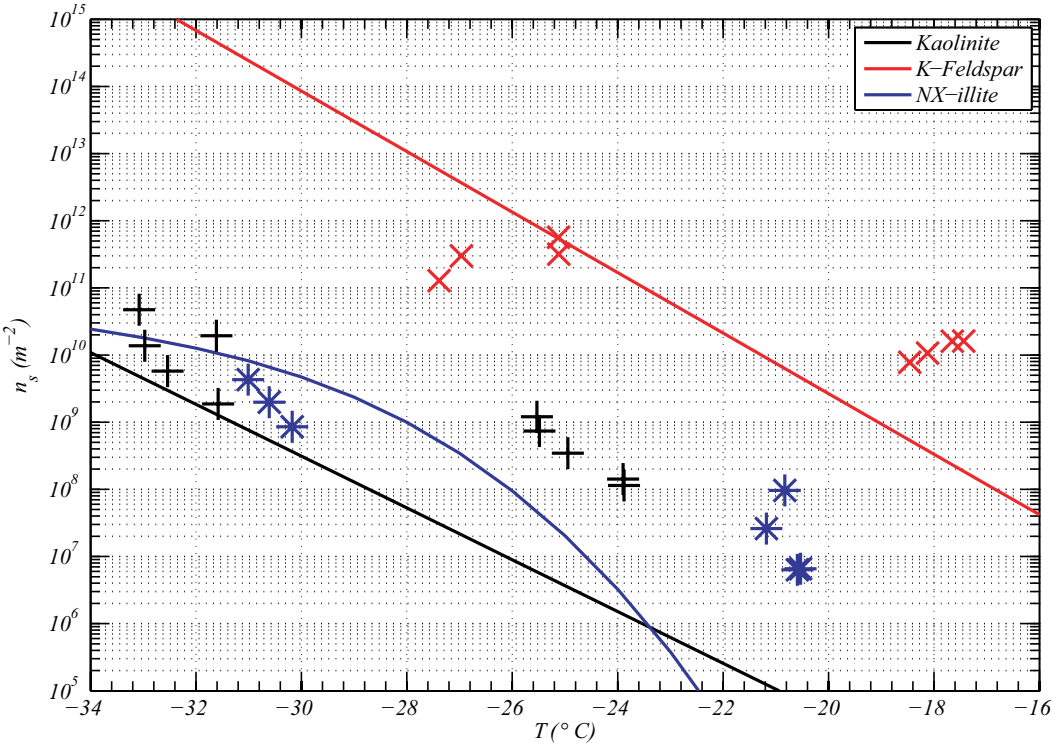

Fig. 8. n_s values from the literature (solid) lines. Blue line is for NX-illite from Broadley et al. (2012); black line is for kaolinite from Murray et al. (2011) and red line is for K-feldspar from Atkinson et al. (2013). The symbols correspond to n_s values derived using Equation 2 with our data in Table 1. The colours correspond to the same mineral particles as the solid lines.

derstand the reason for differences between dry-dispersion and wet-suspension techniques; hence, coagulation model calculations are presented in Section 4.2.2.

4.2.1 Chamber modelling

We operated ACPIM as a cloud parcel model with bin microphysics. The aerosol size distributions were specified as lognormal fits to the observed data from the UHSAS and the WELAS probes (see Table 1). The curves were fitted manually to the data, but fitted the data very well. Since the background aerosol were not ice nuclei we assumed they were hygroscopic aerosol (ammonium sulphate). A single lognormal mode of ammonium sulphate aerosol was used to describe the background aerosol measured during the background experiment while 3 lognormal modes were used to describe the mineral particle size distribution that was measured prior to the experiment. The background aerosol could be clearly distinguished from the mineral particle size distribution by size: the background dis-

tribution was narrow and had a median diameter of ~ 40 nm; whereas the mineral particle distribution was broad and had a median diameter of ~ 400 nm. It was assumed that the mineral dust were composed of a small amount of soluble material, to enable them to act as cloud condensation nuclei (as well as ice nuclei). The model was relatively insensitive to the fraction of soluble material assumed. The parcel model was forced with the observed pressure drop rate and the temperature rate of change was calculated from the conservation of energy (1st law of thermodynamics) for moist air with a heat derivative that depends on the temperature difference between the gas and the chamber walls. In the model, total water content remained constant during an experiment (which was consistent with the condensed mass inferred from the CDP measurements and water vapour concentration measured by a tunable diode laser).

The condensation process was described by the droplet growth equation (Pruppacher and Klett, 1997), with equilibrium vapour pressures described by Köhler theory. Ice nucleation was modelled using the parameterisation of Koop et al. (2000) for homogeneous freezing or, Murray et al. (2011); Broadley et al. (2012); Atkinson et al. (2013) for heterogeneous freezing by the kaolinite, illite or feldspar mineral dust respectively. A criteria was added that a dust particle had to have 5×10^{-14} kg of water condensed before it could act in the immersion / condensation mode—this prevented ice nucleation at conditions that were sub-saturated wrt water, as observed. Once nucleated ice crystals grew according to the ice crystal growth equation (Pruppacher and Klett, 1997), and in this work crystals were assumed to be quasi-spherical with a variable effective density (see Connolly et al., 2012, for details). All derivatives form a large set of coupled ODEs, which were solved using the DVODE solver from Netlib.

The ACPIM model was run for every experiment in Table 1 and the results are summarised as ratios of observed to simulated ice crystal concentrations in Figure 9. The statistics in Figure 9 were calculated from each of the experimental runs for a particular set of experiments. In general it is shown that the parameterisations underestimate the ice crystal concentrations at all temperatures whereas from Figure 8 one would expect the parameterisations to do reasonably well at the lower temperatures. The reason the parameterisations do not to well at low temperatures is because the dry dispersion data suggest that the slope of the n_s vs temperatures curves should be shallower, thus yielding higher values of n_s at the start of the expansion.

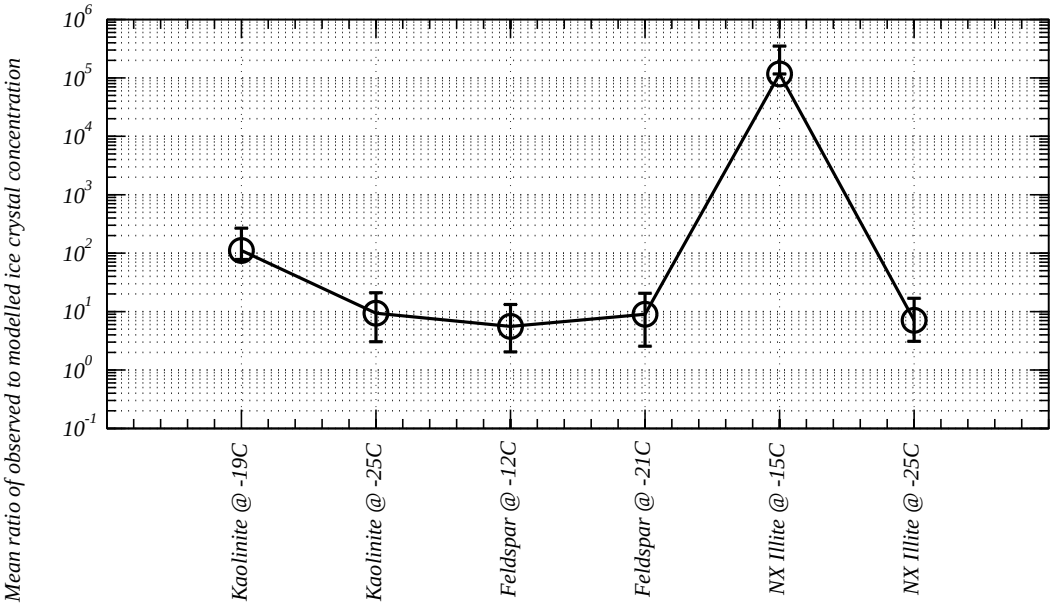

Fig. 9. Figure summarising the results of the ACPIM simulations. The metric shown is the ratio of observed to modelled ice crystal number concentrations averaged over all expansions in a set of experiments. Error bars are 25th and 75th percentiles. The ACPIM model used the parametrisations from Murray et al. (2011); Broadley et al. (2012); Atkinson et al. (2013) for kaolinite, illite and k-feldspar particles respectively.

4.2.2 Coagulation modelling

In the experimental approaches relying on wet suspension, mineral particles are added to a large volume of water and the suspension is stirred for ~ 12 hours with a magnetic stirrer. The drops containing mineral particles in suspension are then either sprayed (in which case pico-litre drops are produced) or pipetted onto a glass slide (in which case micro-litre drops are produced). A few minutes may then elapse before commencing the cooling of drops. Hence, it is possible that coagulation of particles happens, either in the large volume of water, or in the drops before and during the cooling cycle.

We modelled the coagulation of particles within wet-suspensions using the model described in Appendix A. We present the results here neglecting the electric double charge layer that is commonly used to describe inter-particle forces in a colloid (our justification for this is discussed in Section 5.1.1).

Simulations with the coagulation model were performed for 2 hours run-time. We performed simulations for two weight percents (0.005 and 1.000) and also used 3 assumptions

for the size of the water drops that the mineral particles were suspended in. The first was to assume a pico-litre volume drop (1×10^{-15} m^3); the second was to assume a micro-litre volume drop (1×10^{-9} m^3) and the third was to assume an infinite volume of water. The reason for these choices was that they span the range of conditions encountered in the cold stage experiments. We also used different coagulation kernels: one where forces due to Brownian motion were the only forces governing the motion of the particles; and another where Brownian and gravitational settling forces were acting.

Figure 10 shows results from the coagulation model assuming that the forces governing the movement of mineral particles are those due to Brownian motion only. Figure 10(a and b) show that hardly any coagulation occurs within the pico-drops at the weight percents assumed in the calculations. This is evident from the fact that the particle sizes do not change with time. There are just too few particles present for coagulation to be efficient. When micro-litre drops are used (Figure 10(c and d)) we see that the size of the mode shifts to larger sizes. This is significant for the larger weight percent drops where the median size shifts from sub-micron to 10s of microns. The assumption of an infinite volume of water in Figure 10(e and f) yields similar results to the micro-litre model run.

From the results in Figure 10 we have calculated the ratio of mineral particle surface area to the initial mineral particle surface area. These calculations are shown in Figure 11. We have assumed that a collision between to mineral particles yields a mineral particle with the same volume as the other two and that they produce quasi-spherical particles with a fractal dimension of $\sim$2 (Vaezi G et al., 2011, as shown by). Figure 11 shows that, at the highest weight percent in the micro-litre drop, the surface area of the mineral particles quickly drops to ~ 0.1 of the initial value. For the highest weight percent in the pico-litre drop and for the lowest weight percent of the micro-litre drop we see that the surface area available for nucleation is ~ 0.5 of the initial value. Finally, for the lowest weight percent in the pico-litre drop we see no reduction in the available surface area.

Figure 12 shows the same calculation of available surface area vs time when both Brownian motion and gravitational settling influence the coagulation kernel. Similar results to those for the Brownian only kernel are shown for the pico-litre drops and also for the micro-litre at low weight percent; however, for the micro-litre drop at high weight percent we see that the available surface area quickly drops to 0.005 of the initial value. This is in the region required to explain the discrepancies seen in Figure 8.

It should be noted that our simulations of coagulation offer a rough calculation of the re-

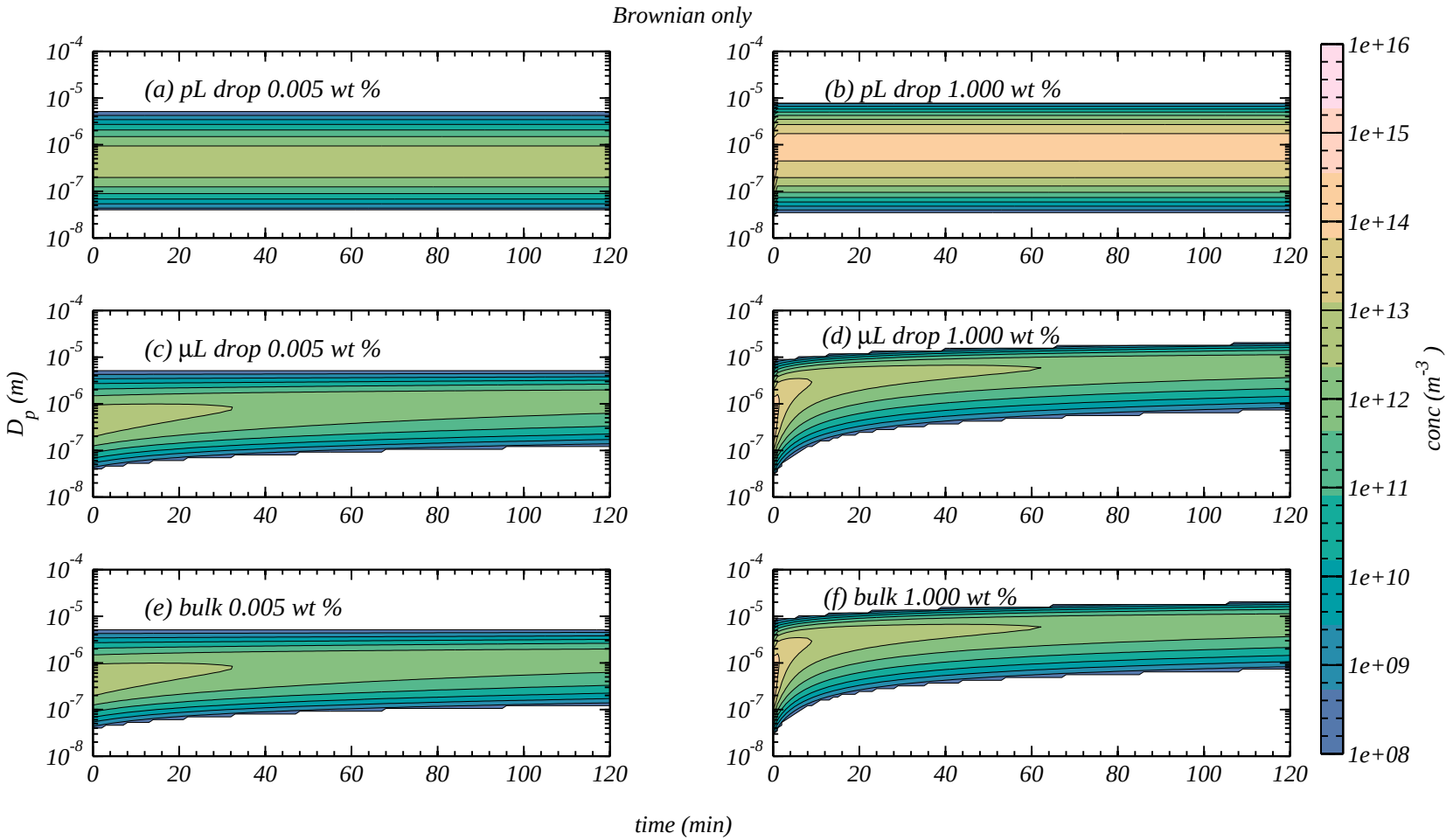

Fig. 10. Numerical model simulations of the coagulation of mineral particles within suspension showing the size distribution evolution vs time. (a) is for a 0.005 wt% suspension inside a pico litre drop; (b) is the same as (a) but for 1.000 wt %; (c) is for a 0.005 wt% suspension inside a micro litre drop; (d) is the same as (c) but for 1.000 wt %; (e) and (f) are the same as (c) and (d) respectively, but for an infinite volume.

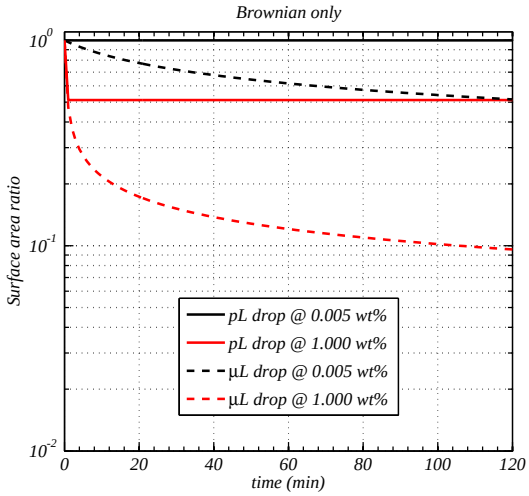

Fig. 11. The evolution of the ratio of particle surface area to initial particle surface area for mineral particles undergoing coagulation in water suspension. The coagulation kernel assumed is that due to collisions arising from Brownian motion only.

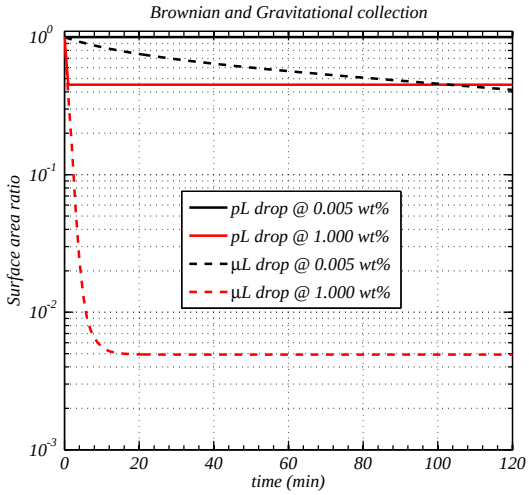

Fig. 12. Same as Figure 11, but with the coagulation due to Brownian motion and gravitational settling.

duction in surface area due to coagulation. However, another important process to consider is the fact that, once aggregated, large particles will sediment out of the suspension; therefore further reducing the available surface area for nucleation. The subsequent calculations of n_s will be biased low because the surface area used to calculate n_s (the original surface area added to the suspension) will be too high.

4.3 Colloid experiments

In order to support our calculations we have conducted experiments where we make up a colloid with 0.1 to 1% wt suspension (either k-feldspar, kaolinite or nx-illite) in ultrapure (18.2 MΩ) water.

We stirred the suspensions for 12 hours using a magnetic stirrer to reproduce the methods of previous ice nucleation studies and then passed them through either 1 μm or 5 μm filters (22mm Cellulose nitrate membrane, Whatman, UK). We found in all cases that this process reduced the absorbance of UV and visible light to that of ultrapure water (UV-Vis spectrometer, Stellarnet,Fla., USA) and, therefore, removed the particles completely to within error of the absorbance measurements. Less than 2ml of suspension was passed through the filter membranes and their effective pore-size would have remained unaltered, this, therefore, suggests that the particles had aggregated from their initial sub-micron sizes to super micron sizes. We also monitored the absorbance of the suspension vs time across the spectrum; at 567 nm, the optimum wavelength with respect to signal to noise, we found it to decrease by a factor of 10 within 90 minutes of sample preparation. This also suggests that sedimentation and aggregation may have occurred.

Laser diffraction (dynamic light scattering) measurements for the kaolinite sample were also conducted using 0.1% wt suspension. In these experiments we varied the pH of the water and also the concentration of ions in solution. The results are summarised in Table 2. These measurements showed that the size distribution of kaolinite particles was sensitive to both the pH and the salt concentration. In all cases the sizes were ~ 1 μm or greater, indicating that aggregation had taken place; however, the extent of the aggregation decreased with increasing pH. At pH 11 the sizes were $\sim 0.8\,\mu$m diameter, whereas at pH 7.5 and lower the sizes were $\sim 3\,\mu$m and higher.

Table 2. Table showing results from dynamic light scattering experiments for the kaolinite sample.

In water (0.1% wt)		
pH	Average diamter (μm)	Standard deviation (μm)
3.5	8.1	3.1
5.5	4.8	0.4
7.5	4.8	0.8
9.5	2.7	0.2
11	1.3	0.1
100 mM NaCl (0.1% wt)		
pH	Average diamter (μm)	Standard deviation (μm)
3.5	4.0	0.4
7.5	3.2	0.3
11	2.0	0.1

5 Discussion

Recently Hiranuma et al. (2014) suggested that there is a discrepancy between the dry-dispersion and wet-suspension methods of determining the ice nucleation efficiency of the clay mineral NX-illite. They offered the explanation that the mineral surface is chemically altered during reaction with water. Their measurements of ion concentrations in water containing NX-illite supported this finding; however, their water was acidic to speed up the breakdown of the mineral surface. Here we find the same result for NX-illite. We also find very similar results for K-feldspar and kaolinite KGa-1b samples. Namely that the dry-dispersion method used predicts higher values of n_s than the previously published results using wet-suspensions at the highest temperatures, but agrees at the lower temperatures. We offer an alternate explanation to that of Hiranuma et al. (2014), which is that the mineral particles coagulate together in suspension and reduce the surface area available for nucleation.

This explanation is also consistent with the discrepancy found at high temperatures: in the wet-suspension methods, the high temperature results use the highest mineral particle weight percents, which are more likely to coagulate. However, Atkinson et al. (2013) show high weight percents (0.8%) in pico-litre drops at lower temperatures that agree with our measurements. We suggest that the reason is that the mineral particles are prevented from coagulation by the stirring process but that they coagulate in the 'few minute' period after

Table 3. Table showing BET specific surface area of the different mineral samples used in this study.

Mineral sample	BET SSA m^2 kg^{-1}	Bulk density (kg m^{-3})	SSA underestimation factor
Kaolinite	11800	2650	~ 2.1
NX-Illite	104200	2770	~ 19.2
K-feldspar	3115[2]	2570	~ 0.53

being pippeted onto the glass side. This may explain (with reference to Figure 12) why the pico-litre drops at high weight percent presented in Atkinson et al. (2013) agrees with our measurements, but the micro-litre drops at the same weight percent do not. Coagulation can occur within micro-litre drops, but tends not to in pico litre drops because they lack sufficient mineral particles for the process to be efficient.

5.1 Does the assumption of spherical particles affect our findings?

We note that Figure 8 is adjusted so that we take account of the specific surface area; however, the process modelling (Figure 9) assumes the surface area of spherical mineral particles. Here we assess whether this affects the main findings. The quoted values for BET specific surface areas of the three samples are shown in Table 3.

We estimate the discrepancy in the assumption that the particles are spherical. The median diameter for the three samples when introduced into the chamber was approximately $D_m = 0.4 \times 10^{-6}$ m. The calculated surface area to mass ratio is then, S:

$$S = \frac{6\cancel{D_m^2}}{\rho \cancel{D_m^3}} \tag{4}$$

$$= \frac{6}{\rho D_m} \tag{5}$$

We may then calculate the SSA underestimation factor, which is the ratio of the SSA to the value of S. Table 3 shows that the assumption of spherical particles likely underestimates the surface area for the kaolinite and NX-illite samples by factors of ~ 2 and ~ 20 respectively. For the K-feldspar the assumption of sphericity overestimates the surface area by a factor of ~ 2. The underestimation is because the particles are platelets so measured optical size is closer to $\frac{\pi D^2}{2}$ (area of a disk) instead of πD^2 (area of a sphere). It should be noted that these values are not large enough to significantly affect the conclusions from Figure 9.

[2] 3.5 times that of 890

5.1.1 Colloidal forces in suspensions

The coagulation modelling in Section 4.2.2 neglected the force of repulsion due to the electric double charge layer (see Appendix B and C for details). Layered mineral particles like kaolinite consist of alternating silca (tetrahedral) and alumina (octahedral) layers, which are bonded together. The tetrahedral faces have a net negative charge due to isomorphic substitution of silicon ions by ions with a lower charge, whereas the edges and octahedral faces have charges that depend on the pH of the solution.

When placed in suspension the minerals develop a double charge layer by attracting positive ions (counter-ions) to the surface. The double charge layer can result in the particles being colloidally stable because of the effective like-charge Coulomb interaction between two particles. The sign and magnitude of the charge layer can be quantified by inferring the zeta-potential from measurements of electro-phoresis.

We now provide some justification for the decision to neglect it. Elimelech et al. (2000) have shown that the ζ-potential is a relatively insignificant factor in predicting the transport / sedimentation of particles when there is heterogeneity in the surface of the colloidal material. This is reasonable since the ζ-potential is only a bulk measurement of the charge on a population of particles.

Tombácz and Szekeres (2006) have since shown that kaolinite has surface charge heterogeneity due to the mineral having permanent charges on the tetrahedral silica faces and pH dependent charges on the crystal edges and also the octahedral alumina faces. In the paper by Tombácz and Szekeres (2006), kaolinite samples were heavily processed to remove the large particle sizes and any other contamination; however, surface charge heterogeneity still persisted.

The kaolinite clay is a 1:1 layer clay consisting of single layers of silica and alumina that are bonded together. The silica layers have isomorphic substitution; hence, carry a net negative charge. However, the faces of alumina and edges of the crystal may undergo hydrolysis and hence carry pH dependent charges (Tombácz and Szekeres, 2006). Tombácz and Szekeres (2006, their Fig. 7) show that, at pH 7, these alumina and silica groups (as inferred through a linear combination of their zeta potential) may have an overall charge close to zero. Hence, there is surface charge heterogeneity in clay minerals. Indeed Schofield and Samson (1954) had noted previously that ‘edge to face’ coagulation (or flocculation) occurs in kaolinite samples.

Berka and Rice (2005) have shown that kaolinite can be colloidally stabilized at particle concentrations similar to those under consideration here ($\sim 10^{16}$ m^{-3}); however, their results are at pH of 9.5, where the alumina also carries high negative charge; hence, it should be expected that kaolinite will be colloidally stabilized to some extent at pH 9.5. Our own dynamic light scattering measurements confirm that this is the case (Table 2).

6 Conclusions

Experiments were conducted in the Manchester Ice Cloud Chamber facility to look at ice nucleation in the condensation mode. Three dusts were investigated: kaolinite, illite, and feldspar, and each dust was examined at relatively high and low temperatures. The primary goal of this study was to reconcile dry-dispersion methods of quantifying ice nucleation on mineral dusts with those using wet-suspension.

Observations revealed feldspar to be the most efficient dust at nucleating ice (Figure 8) in agreement with Atkinson et al. (2013), followed by illite, then kaolinite. Thus our data are qualitatively in agreement with previous findings. However, they all showed a discrepancy at the higher temperatures; the dry dispersion methods always showed higher values of n_s than the wet-suspension methods.

Using the ACPIM numerical model to simulate the cloud chamber with ice nucleation parameterisations provided by Murray et al. (2011); Broadley et al. (2012), ice concentrations for all dusts were underestimated relative to observations. The reason for this was that the slope of the n_s vs temperature curves were determined to be less steep in our measurements than the wet-suspension methods. Hence, the reason the model under-predicted the ice crystal concentration at lower temperatures was because the values of n_s from the parameterisations were too low at the start of the experiment. Thus too few ice crystals were nucleated and by the time the lower temperatures were reached the Bergeron-Findeison process had led to the evaporation of the drops.

Modelling of coagulation in suspension showed that it may be a pathway to significantly reduce the surface area of mineral particles and hence would reduce the effective n_s. This is confirmed by separate experiments passing the suspensions through filters after initial dispersion and also through dynamic light scattering.

To explain the discrepancy between dry-dispersions and wet-suspensions we suggest the following:

- During the stirring process feldspar particles do not coagulate strongly and remain in suspension.
- Illite and kaolinite particles may behave differently and could coagulate during the stirring process.
- At high concentrations ~ 1.000 wt % coagulation is more likely to happen.
- As the drops are either sprayed, or pippetted onto the glass slide the mineral particles within the drops may start to coagulate.
- In pico-litre drops there are insufficient mineral particles, even at 1.000 wt %, to result in significant coagulation.
- In micro-litre drops there are enough mineral particles to result in significant coagulation, and reduction of surface area in the drops. This reduction increases with increasing wt % of mineral particles.
- The data points for n_s vs temperature derived from these experiments more closely agree with those derived for natural dusts by Niemand et al. (2012).
- The dry-dispersion techniques suggest that mineral particles are more efficient than the wet-suspension derived parameterisations suggest, especially at relatively high temperatures.

Appendix A Modelling coagulation in suspension

We adopted the semi-implicit numerical algorithm for treating the coagulation process (pp 438 Jacobson, 1999). This method conserves total particle volume and approximately conserves the monomer concentration. The algorithm is written as follows:

$$v_{k,t} = \frac{v_{k,t-1} + dt \sum_{j=1}^{k} \left(\sum_{i=1}^{k-1} f_{i,j,k} \beta_{i,j} v_{i,t} n_{j,t-1} \right)}{1 + dt \sum_{j=1}^{N_B} \left(1 - f_{k,j,k}\right) \beta_{k,j} n_{j,t-1}} \tag{A1}$$

with $n_k = \frac{v_k}{\nu_k}$ and:

$$f_{i,j,k} = \begin{cases} \left(\frac{\nu_{k+1}-V_{i,j}}{\nu_{k+1}-\nu_k}\right)\frac{\nu_k}{V_{i,j}} & \nu_k \leq V_{i,j} < \nu_{k+1} \text{ if } k < N_B \\ 1 - f_{i,j,k-1} & \nu_{k-1} < V_{i,j} < \nu_k \text{ if } k > 1 \\ 1 & V_{i,j} \geq \nu_k \text{ if } k = N_B \\ 0 & \text{all other cases} \end{cases} \tag{A2}$$

Equation A1 shows that the solution at the next time-step depends on the solution at that time-step; hence, the method is an 'implicit' method; however, the algorithm is solve sequentially in discrete bins such that the solution at the next time-step is always known.

The variable β is the coagulation kernel of two interacting particles (m^3 $particle^{-1}$ s^{-1}). When by the concentration of particles in a discrete bin it gives the rate of the number of particle interactions. We assume it can be described by the sum of a kernel due to Brownian diffusion and that due to gravitational settling. For Brownian the diffusion the kernel takes the form:

$$\beta(i,j) = 4\pi \left(r_i + r_j\right)\left(D_{p,i} + D_{p,j}\right) \tag{A3}$$

where $D_{p,i}$ and $D_{p,j}$ are particle diffusion coefficients:

$$D_{p,i} = \frac{k_B T}{6\pi r_i \eta_w} \tag{A4}$$

following Einstein (1956). This model assumes that each Brownian collision results in a sticking event.

For gravitational settling the kernel takes the form:

$$\beta(i,j) = E_{i,j}\pi \left(r_i + r_j\right)^2 \left|u_{t,i} - u_{t,j}\right| \tag{A5}$$

Appendix B Interaction potential of minerals in suspension

A particle suspended in water will generally form a double charge layer by accumulation of ions.

The potential energy of the electrical double layer interaction between two spheres may be written:

$$V_R = \left(\frac{\pi\epsilon R_1 R_2}{R_1 + R_2}\right)\left(\zeta_1^2 + \zeta_2^2\right)\left(\frac{2\zeta_1\zeta_2}{\zeta_1^2 + \zeta_2^2}p + q\right) \tag{B1}$$

where R_1 and R_2 are the radii of the two interacting particles; ϵ is the electric permittivity; $\zeta_{1,2}$ are the zeta potentials of the interacting particles.

$$p = \ln\left(\frac{1+\exp\left(-\kappa x\right)}{1-\exp\left(-\kappa x\right)}\right) \tag{B2}$$

450

$$q = \ln\left(1-\exp\left(-2\kappa x\right)\right) \tag{B3}$$

where x is the shortest distance between to particles and κ^{-1} is the Debye length:

$$\kappa^{-1} = \sqrt{\frac{\epsilon k_B T}{N_A e^2 \sum Z^2 m_i}} \tag{B4}$$

where k_B is Boltzmann's constant; N_A is Avogadros' number, $e = 1.6 \times 10^{-19}$ C is the charge on an electron; Z and m_i are the valence and molar concentration (moles per cubic metre) of ions; and T is the temperature.

In addition to the electrical double layer potential we also consider van der Waals, which is given by London's equation:

$$\begin{aligned} V_A = -\frac{A_{132}}{6}\Bigg(&\frac{2R_1R_2}{\left[R_1+R_2+x\right]^2+\left[R_1+R_2\right]^2} \\ &+\frac{2R_1R_2}{\left[R_1+R_2+x\right]^2+\left[R_1-R_2\right]^2} \\ &+\ln\left[\frac{\left[R_1+R_2+x\right]^2+\left[R_1+R_2\right]^2}{\left[R_1+R_2+x\right]^2+\left[R_1-R_2\right]^2}\right]\Bigg) \end{aligned} \tag{B5}$$

here, A_{132} is the Hamaker constant for interaction between particle 1, particle 2 in medium 3. Individual Hamaker constants are as follows: for mineral particles we use A_1 and $A_2 = 6.8 \times 10^{-19}$ J; whereas for pure water we use $A_3 = 7 \times 10^{-21}$ J. A_{132} can be estimated (source) from the Hamaker constants for pure components:

$$A_{132} \cong \left(\sqrt{A_1}-\sqrt{A_3}\right)\left(\sqrt{A_2}-\sqrt{A_3}\right) \tag{B6}$$

The total potential for the interaction is given by the sum of van der Waals and the double

455 electric charge layer: $V_T = V_A + V_R$.

Appendix C Coagulation kernel with interaction potential

As described in Crowe (2006, Section 6.3.1.2) the coagulation kernel can be corrected for the effect of an external, conservative force field. Here, 'external' refers to the force field being external to the process considered in the uncorrected kernel. The correction is to divide the kernel by the factor:

$$Q = (R_i + R_j) \int_0^\infty \frac{\exp\left[\frac{V_T(x)}{k_B T}\right]}{x^2} dx \tag{C1}$$

We define the enhancement factor over the Brownian kernel, W, as the ratio of Q calculated with the interaction potential in Equations B1 and B5 to that calculated by van der Waals alone (B5). This enhancement factor is shown in Figure 13 for two, spherical, $0.1\,\mu$m diameter, particles having different values of the zeta-potential.

Figure 13 shows that two particles may come together if the zeta-potential of one of the particles has a magnitude less than a threshold of $\sim$ 10 mV. However, mineral particles are not spheres and exhibit patch-wise heterogeneity in their surface potential (see Section 5.1.1). Hence, we argue that for measured bulk zeta-potentials of -20 mV there may be enough heterogeneity in the sample, in addition to patch-wise heterogeneity, to lead to colloidal instability.

In addition Figure 13 also shows that the enhancement factor may be greater than unity even when the particles have like change. This is seen most clearly at values of $\zeta_1 \cong -20$ mV and $\zeta_2 \cong 0$ mV, where the enhancement factor is ~ 5. This behaviour is because the interaction between the two spheres produces induced charges, and has been observed experimentally in other studies.

Acknowledgements. This work was funded by the NERC ACID-PRUF programme, grant code NE/I020121/1. We also acknowledge funding from the EU FP7-ENV-2013 programme "impact of Biogenic versus Anthropogenic emissions on Clouds and Climate: towards a Holistic UnderStanding" (BACCHUS), project (number 603445). Ben Murray is acknowledged for providing the mineral particle samples sourced from the clay mineral society.

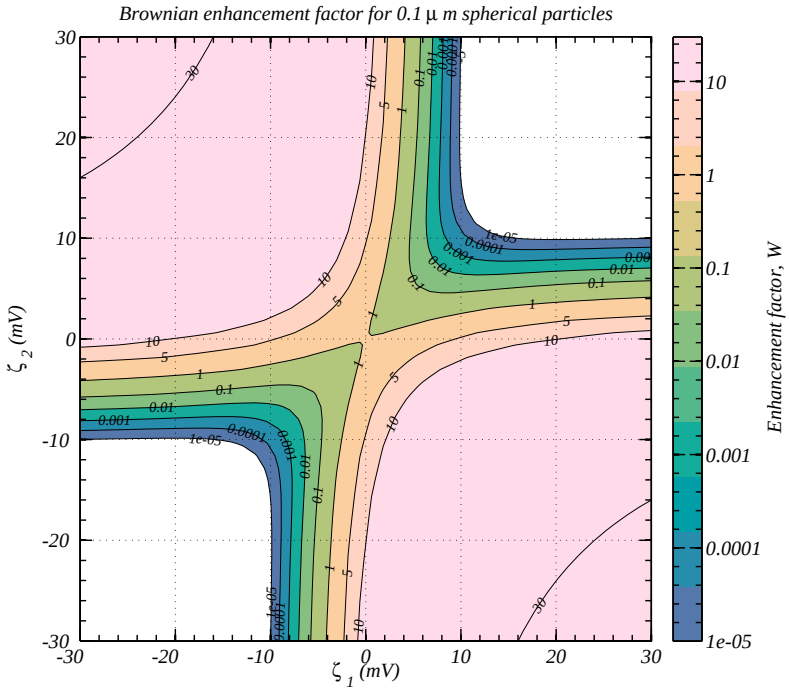

Fig. 13. The enhancement factor of the Brownian collision kernel for two spherical particles in pure water as a function of the zeta-potential of both particles.

References

Atkinson, J. D., Murray, B. J., Woodhouse, M. T., Whale, T. F., Baustian, K. J., Carslaw, K. S., Dobbie, S., O'Sullivan, D., and Malkin, T. L.: The importance of feldspar for ice nucleation by mineral dust in mixed-phase clouds, Nature, 498, 355–358, 2013.

Berka, M. and Rice, J. a.: Relation between aggregation kinetics and the structure of kaolinite aggregates., Langmuir : the ACS journal of surfaces and colloids, 21, 1223–9, doi:10.1021/la0478853, http://www.ncbi.nlm.nih.gov/pubmed/15697264, 2005.

Broadley, S. L., Murray, B. J., Herbert, R. J., Atkinson, J. D., Dobbie, S., Malkin, T. L., Condliffe, E., and Neve, L.: Immersion mode heterogeneous ice nucleation by an illite rich powder representative of atmospheric mineral dust, Atmos. Chem. Phys., 12, 287–307, 2012.

Connolly, P. J., Flynn, M. J., Ulanowski, Z., Choularton, T. W., Gallagher, M. W., and Bower, K. N.: Calibration of the Cloud Particle Imager Probes using Calibration beads and Ice Crystal Analogs: The depth-of-field, Journal of Atmospheric and Oceanic Technology, 24, 1860–1879, 2007.

Connolly, P. J., Möhler, O., Field, P. R., Saathoff, H., Burgess, R., Gallagher, M. W., and Choularton, T. W.: Studies of heterogeneous freezing by three different desert dust samples, Atmos. Chem. Phys., 9, 2805–2824, 2009.

Connolly, P. J., Emersic, C., and Field, P. R.: A laboratory investigation into the aggregation

efficiency of small ice crystals, Atmospheric Chemistry and Physics, 12, 2055–2076, doi: 10.5194/acp-12-2055-2012, http://www.atmos-chem-phys.net/12/2055/2012/, 2012.

Crowe, C. T.: MULTIPHASE FLOW HANDBOOK, City, 1218, 6092–101, doi:10.1016/j.chroma.2011.01.063, http://www.ncbi.nlm.nih.gov/pubmed/21324465, 2006.

Einstein, A.: Investigations on the theory of the Brownian movement, Dover edit, 1956.

Elimelech, M., Nagai, M., Ko, C.-H., and Ryan, J. N.: Relative Insignificance of Mineral Grain Zeta Potential to Colloid Transport in Geochemically Heterogeneous Porous Media, Environ. Sci. Technol., 34, 2143–2148, 2000.

Glaccum, R. A. and Prospero, J. M.: Saharan aerosol over the tropical north atlantic – mineralogy, Mar. Geol., 37, 295–321, 1980.

Hiranuma, N., Augustin-Bauditz, S., Bingemer, H., Budke, C., Curtius, J., Danielczok, A., Diehl, K., Dreischmeier, K., Ebert, M., Frank, F., Hoffmann, N., Kandler, K., Kiselev, A., Koop, T., Leisner, T., Möhler, O., Nillius, B., Peckhaus, A., Rose, D., Weinbruch, S., Wex, H., Boose, Y., DeMott, P. J., Hader, J. D., Hill, T. C. J., Kanji, Z. a., Kulkarni, G., Levin, E. J. T., McCluskey, C. S., Murakami, M., Murray, B. J., Niedermeier, D., Petters, M. D., O'Sullivan, D., Saito, A., Schill, G. P., Tajiri, T., Tolbert, M. a., Welti, A., Whale, T. F., Wright, T. P., and Yamashita, K.: A comprehensive laboratory study on the immersion freezing behavior of illite NX particles: a comparison of seventeen ice nucleation measurement techniques, Atmospheric Chemistry and Physics Discussions, 14, 22 045–22 116, doi:10.5194/acpd-14-22045-2014, http://www.atmos-chem-phys-discuss.net/14/22045/2014/, 2014.

Jacobson, M. Z.: "Fundamentals of atmospheric modelling", "Cambridge University Press", 1999.

Kandler, K., Benker, N., Bundke, U., Cuevas, E., Ebert, M., Knippertz, P., Rodriguez, S., Schutz, L., and Weinbruch, S.: Chemical composition and complex refractive index of Saharan Mineral Dust at Izana, Tenerife (Spain) derived by electron microscopy, Atmos. Env., 41, 8058–8074, doi:doi:10.1016/j.atmosenv.2007.06.047, 2007.

Koop, T., Luo, B., Tsias, A., and Peter, T.: Water activity as the determinant for homogeneous ice nucleation in aqueous solutions, Nature, 406, 611–614, 2000.

Kumar, P., Sokolik, I. N., and Nenes, A.: Parameterization of cloud droplet formation for global and regional models: including adsorption activation from insoluble CCN, Atmospheric Chemistry and Physics Discussions, 8, 16 851–16 890, doi:10.5194/acpd-8-16851-2008, 2008.

Murray, B. J., Broadley, S. L., Wilson, T. W., Atkinson, J. D., and WIlls, R. H.: Heterogeneous freezing of water droplets containing kaolinite particles, Atmos. Chem. Phys., 11, 4191–4207, 2011.

Niemand, M., Möhler, O., Vogel, B., Vogel, H., Hoose, C., Connolly, P. J., Klein, H., Bingemer, H., DeMott, P. J., Skotzki, J., and Leisner, T.: A particle-surface-area-based parameterisation of immersion freezing on mineral dust particles, Journal of the Atmospheric Sciences, 69, 2012.

Pruppacher, H. R. and Klett, J. D.: Microphysics of clouds and precipitation, "Kluwer Academic

Press", "Norwell", 1997.

Schofield, R. K. and Samson, H. R.: Flocculation of kaolinite due to the attraction of oppositely charged crystal faces, Discussions of the Faraday Society, 18, 135–145, doi:10.1039/DF9541800135, 1954.

Tombácz, E. and Szekeres, M.: Surface charge heterogeneity of kaolinite in aqueous suspension in comparison with montmorillonite, Applied Clay Science, 34, 105–124, doi:10.1016/j.clay.2006.05.009, http://linkinghub.elsevier.com/retrieve/pii/S0169131706001232, 2006.

Vaezi G, F., Sanders, R. S., and Masliyah, J. H.: Flocculation kinetics and aggregate structure of kaolinite mixtures in laminar tube flow., Journal of colloid and interface science, 355, 96–105, doi:10.1016/j.jcis.2010.11.068, http://www.ncbi.nlm.nih.gov/pubmed/21208625, 2011.

Vali, G.: Supercooling of Water and Nucleation of Ice (Drop Freezer), American Journal of Physics, 39, 1125–1128, 1971.

Nomenclature

β Coagulation kernel (m^3 $particle^{-1}$ s^{-1}), page 26

ϵ Permittivity of water (F m^{-1}), page 27

η_w Viscosity of water $\sim 8.9 \times 10^{-4}$ Pa s, page 26

κ Reciprocal of Debye length (m^{-1}), page 27

ν The volume of a single particle in a bin (m^3), page 26

ζ_1 zeta potential of particle 1 (V), page 27

ζ_2 zeta potential of particle 2 (V), page 27

A_1, A_2 Hamaker constant for particles 1 and 2 (6.8×10^{-19} J), page 27

A_3 Hamaker constant for water (7×10^{-21} J), page 27

A_{132} Hamaker constant for interaction between particle 1 and 2 in medium 3, page 27

$D_{p,i}$ Particle diffusion coefficient (Stokes-Einstein coefficient) for bin i (m^2 s^{-1}), page 26

e Charge on electron ($\sim 1.6 \times 10^{-19}$ C), page 27

k_B Boltzmann's constant, 1.381×10^{-23} m^2 kg s^{-2} K^{-1}, page 26

m_i Molar concentration of ions (mol m^{-3}), page 27

N_A Avogadros number (6.02×10^{23}), page 27

N_B The number of bins, page 26

R_1 Radius of particle 1 (m), page 27

R_2 Radius of particle 2 (m), page 27

$r_{i,j}$ The radius of a particle in bin i or j (m), page 26

T Temperature (K), page 27

u Terminal velocity of particle in fluid (m s^{-1}), page 26

V The volume of the bin edges (m^3), page 26

v The number concentration of a particle in a bin (m^{-3}), page 26

v The total volume all particles in a bin (m^3 m^{-3}), page 26

V_A van der Waals interaction potential (V), page 27

V_R Interaction potential between two particles (V), page 27

V_T Sum of all interaction potentials (V), page 28

W Correction factor for particles interacting with potential, page 28

x Distance between two particles (m), page 27

Z Valence of dissociation, page 27